FlexBRDF: A Flexible BRDF Correction for Grouped Processing of Airborne Imaging Spectroscopy Flightlines

Natalie Queally[1], Zhiwei Ye[1], Ting Zheng[1], Adam Chlus[1], Fabian Schneider[2], Ryan P. Pavlick[2], Philip A. Townsend[1]

[1]Department of Forest and Wildlife Ecology, University of Wisconsin-Madison, 1630 Linden Drive, Madison, WI 53706, USA. [2]Jet Propulsion Laboratory, California Institute of Technology, 4800 Oak Grove Drive, Pasadena, CA 91011, USA.

Corresponding author: Natalie Queally (queally@wisc.edu)

Key Points:

- FlexBRDF corrects BRDF effects in groups of adjacent flightlines to minimize between-image spectral differences
- Interpolation of NDVI bins prevents between-bin edges
- FlexBRDF is highly customizable and performed well for a variety of sites and sensors

Abstract

Bidirectional reflectance distribution function (BRDF) effects are a persistent issue for the analysis of vegetation in airborne imaging spectroscopy data, especially when mosaicking results from adjacent flightlines. With the advent of large airborne imaging efforts from NASA and the US National Ecological Observatory Network (NEON), there is increasing need for methods that are both flexible and automatable across numerous images with diverse land cover. FlexBRDF corrects for BRDF effects in groups of flightlines, with key user-selectable features including kernel selection, land cover stratification (we employ NDVI), and use of a reference solar zenith angle (SZA). We demonstrate FlexBRDF using a series of nine long (150-400 km) AVIRIS-Classic flightlines collected on 22 May 2013 over Southern California, where rough terrain, diverse land cover, and a wide range of solar illumination yield significant BRDF effects, and then test the approach on additional AVIRIS-Classic data from California, AVIRIS-Next Generation data from the Arctic and India, and NEON imagery from Wisconsin. Based on comparisons of overlap areas between adjacent flightlines, correction algorithms built from multiple flightlines concurrently performed better than corrections built for single images (RMSE improved up to 2.3% and mean absolute deviation 2.5%). Standardization to a common SZA among a group of flightlines also improved performance. While BRDF corrections tailored to individual sites may be preferred for local studies, FlexBRDF is compatible with bulk processing of large datasets covering diverse land cover needed for calibration/validation of forthcoming spaceborne imaging spectroscopy missions.

Plain Language Summary

Airborne imaging spectroscopy data are used to map a suite of canopy functional traits, their functional diversity, and species composition. However, variation in sun and solar geometry and land cover type can cause unwanted brightness gradients across an image. In studies where multiple images are mosaicked or where reflectances from multiple images will be compared, image brightness gradients may significantly confound analyses. Here we present FlexBRDF, a flexible correction technique that concurrently removes brightness artifacts in groups of flightlines. We tested our method across a diverse set of ecosystems and provide a generalized set of model parameters, which can be easily customized to fit the user's needs. The method is suitable for application to large airborne campaigns in which site-specific corrections are infeasible, and which provide baseline data for current and future satellite missions.

1 Introduction

Imaging spectroscopy, also known as hyperspectral remote sensing, has become a critical technology for understanding the dynamics of vegetation, including functional traits (Asner, Martin, et al., 2015; Singh et al., 2015; Wang et al., 2019, 2020), vegetation type, composition and diversity (Colgan et al., 2012; Li et al., 2005; Roberts et al., 1998; Schneider et al., 2017), senescent vegetation fraction (Dennison et al., 2019; Guerschman et al., 2009; Roberts et al., 1993), photosynthetic capacity (Serbin et al., 2015), and disturbance and stress (Asner, Brodrick, et al., 2016; Veraverbeke et al., 2014). Current and forthcoming spaceborne missions such as Surface Biology and Geology (NASEM, 2018), CHIME (Nieke & Rast, 2018), HiSUI (Iwasaki

et al., 2011), PRISMA (Loizzo et al., 2018), and EnMap (Stuffler et al., 2007) will offer unprecedented capacity to characterize Earth's terrestrial ecosystems, which is critical given rapid ongoing losses in biodiversity and climate change (Jetz et al., 2016; Schimel et al., 2020). Calibration and validation of global missions such as SBG will require extensive airborne imaging spectroscopy to provide sufficient spatial and temporal coverage of necessary biological and physical measurements that are not logistically feasible from in-situ sampling. Such airborne campaigns have increased significantly in recent years, with efforts including the U.S. National Ecological Observatory Network (NEON) (Kampe, 2010), and NASA airborne imaging spectroscopy campaigns such as the Arctic Boreal Vulnerability Experiment (Kasischke et al., 2010), India (Bhattacharya et al., 2019) and Europe (Hueni et al., 2018) campaigns, and the California Western Biodiversity Time Series (WBTS, citation) (Lee et al., 2015). In addition to providing critical baseline data for satellite missions, airborne missions currently also provide important high resolution data to prototype development of algorithms and data sets for those missions.

The airborne data sets needed to support satellite campaigns have a number of important conditions. First, these airborne campaigns must cover areas larger than a single airborne flightline, necessitating datasets comprised of multiple flightlines covering a flight box over areas of interest. As well, consistent retrieval of spectral surface reflectance is necessary for producing reliable and comparable maps of derived data products, both across multiple flightlines in a single geographic area and for scenes across sites. Analysis of data from multiple flightlines requires consistent implementation of atmospheric correction, but bidirectional reflectance distribution function (BRDF) effects also strongly influence brightness across images as a function of solar and sensor view angles as well as surface anisotropy (Nicodemus et al., 1977; Schaepman-Strub et al., 2006). In studies where multiple flightlines must be mosaicked for analysis or where retrievals from across multiple flightlines are to be compared, cross-track brightness gradients due to BRDF may significantly confound analyses. BRDF effects are most apparent on the seams between adjacent images, and are manifested as increased brightness on one side of the flightline relative to the other due to sun-sensor-target geometry (Fig. 1). Thus, BRDF correction is used to approximate a constant brightness level corrected to a nadir view angle. This work was motivated by the observation that many BRDF correction approaches for airborne hyperspectral imagery sufficiently address within-flightline brightness gradients without addressing between-flightline variations, which may yield undesirable artifacts in subsequent mosaics or derived products. As such, it is important to ensure that the corrections further account for differences associated with images collected with differing solar geometries.

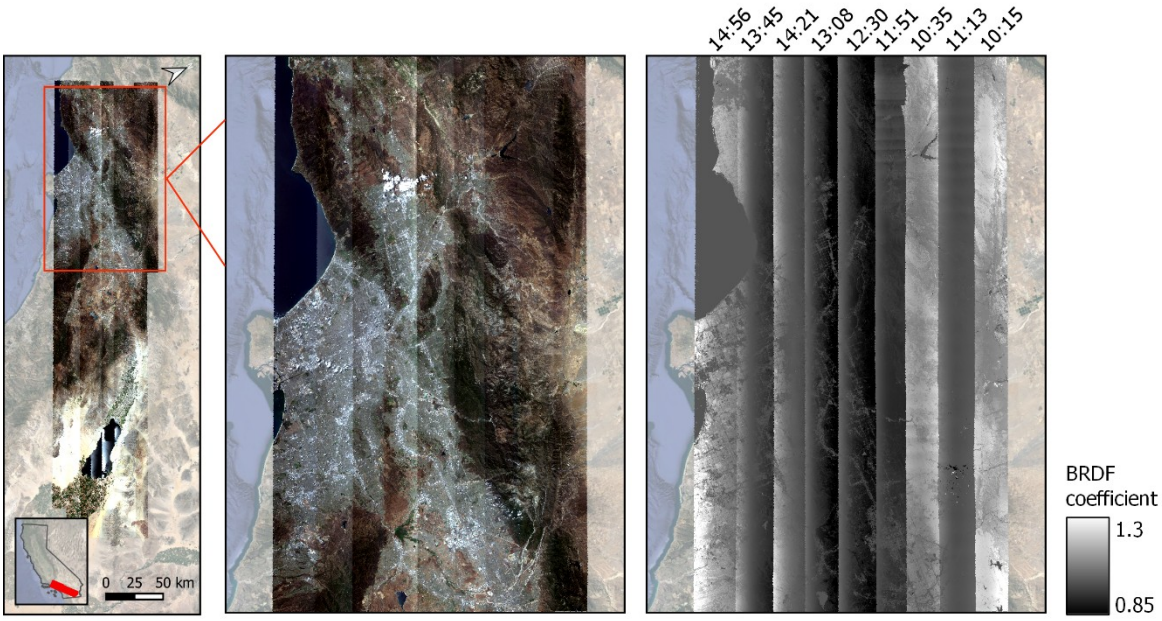

Figure 1. BRDF effects manifest as exceptional brightness and darkness on either end of an image. The middle shows an uncorrected, true-color mosaic. For illustration, the right panel shows BRDF correction coefficients derived in this paper for a sample band (660 nm). Flightlines are labeled by their local acquisition time. The full flight box is shown on the left.

Here we present a flexible, automated approach to BRDF correction optimized for vegetation called FlexBRDF that is suitable for correcting multiple adjacent flightlines based on the combined sun-sensor-target reflectance characteristics across all lines in a flight box acquired on the same day. To minimize shadowing effects from steep terrain, all testing was conducted on topographically-corrected reflectance data using the sun-canopy-sensor + C (SCS+C) topographic correction method outlined in Soenen et al. (2005). FlexBRDF is built upon the Ross-Li kernel-driven semi-empirical BRDF correction method, which implements a set of kernels approximated from physical models to describe different BRDF shapes (Wanner et al., 1995). The BRDF model is a linear combination of geometric, volumetric, and isotropic terms. Collectively, these terms incorporate the geometric structure of reflectors and shadowing effects, the volumetric scattering across randomly distributed facets (such as leaves), and the isotropic scattering contribution (i.e., uniform scattering in all directions) (Roujean et al., 1992).

Within-image BRDF effects are caused by sun and sensor geometries and their interaction with land cover type (Nicodemus et al., 1977; Schaepman-Strub et al., 2006), which influences the geometric and volumetric terms in the BRDF model. To address this, BRDF correction methods commonly use a pre-classification scheme to stratify the BRDF correction by cover type with assumed similarities in crown structure (Colgan et al., 2012; Jensen et al., 2018; Jia et al., 2020; Schläpfer et al., 2015; Weyermann et al., 2015), but this is not practical across large aerial campaigns covering a wide range of vegetation types that may be imaged at different spatial resolutions. FlexBRDF avoids use of an ancillary land cover dataset by stratifying images using the normalized difference vegetation index (NDVI), a common measure of vegetation greenness. The benefit to a widely-used index such as NDVI over a pre-classification for

stratification is that it is continuous (i.e., pixels with similar NDVI values are more likely to be alike than not) and, as a ratio, reduces influence of BRDF (Buchhorn et al., 2016) for stratification compared to pre-classification, which would be performed on uncorrected imagery. Significantly, NDVI enables interpolation of BRDF coefficients between stratification bins, which is not possible using a discrete pre-classification approach. Here we test a range of approaches to NDVI binning, including a dynamic binning strategy that provides flexibility for flightlines of varying land cover heterogeneity.

Flightlines collected within a flight box can cover a range of illumination conditions and vegetation types across the solar window of acquisitions, such that long acquisition flights in areas with high landscape variation may not exhibit consistent BRDF corrections for individually corrected lines in a flight box. FlexBRDF addresses multiple flightline issues in two ways. First, FlexBRDF corrects an entire flight box as a group rather than on a flightline-by-flightline basis, as in Colgan et al. (2012). Second, FlexBRDF accounts for the variation in solar and sensor geometries as data within a flight box are collected over several hours by providing a range of options to select a reference solar zenith angle for the BRDF correction, which is likewise necessary when integrating analyses from flightlines collected under widely varying illumination conditions (Chen et al., 1999; Colgan et al., 2012; Weyermann et al., 2015).

We demonstrate the generality of FlexBRDF across complex landscapes including Mediterranean, temperate and Arctic biomes using airborne imaging spectroscopy data from NASA's 224-band whiskbroom AVIRIS-Classic (Green et al., 1998) and data from several nearly identical 480-band pushbroom sensors including AVIRIS-Next Generation (NG) (Hamlin et al., 2011) and the U.S. National Ecological Observatory Network (NEON) Airborne Observation Platform (AOP) (Kampe, 2010). These instruments image the visible to shortwave infrared spectrum (~380 - 2500 nm) with ±17-18° field of view. These sensors typically collect several long, narrow image strips (subsequently referred to as flightlines) for a given target area (subsequently referred to as a flight box). FlexBRDF was initially developed for a Southern California flight box and applied to subsequent boxes in India, Wisconsin, Alaska, and Yosemite, CA with favorable results. FlexBRDF is open-source and available from GitHub as part of our HyTools toolkit, and has numerous options for topographic correction method, BRDF kernel combinations, vegetation index, binning strategy, and choice of reference solar zenith angle.

2 Study Area and Data

We initially developed FlexBRDF using imagery collected on 22 May 2013 by AVIRIS-Classic for a Southern California flight box that has been routinely flown -- sometimes multiple times per year -- since 2013 (Lee et al., 2015). Images from this flight box exhibit significant brightness differences across flightlines (Fig. 1). In addition, this flight box presents multiple challenges requiring a robust BRDF correction approach: very long flightlines collected across five hours spanning a range of illumination angles, as well as diverse vegetation and considerable topography. The box stretches from the Pacific Ocean to the Salton Sea, with a range of elevation spanning -70 - 3068 m a.s.l., and contains prominent geological features such as the Santa Monica and San Gabriel Mountains, as well as the densely populated city of Los Angeles. Atmospherically-corrected surface reflectance data were accessed through the AVIRIS Data Portal (https://aviris.jpl.nasa.gov/dataportal/). We used nine overlapping flightlines, with spatial resolutions ranging from 14.4 m to 15.8 m, and a spectral resolution of 10 nm at 224 wavebands from 400 to 2500 nm (Green et al., 1998). For AVIRIS-Classic, FlexBRDF used L1B

observation geometry data (specifically, files labelled obs_ort) and L2 surface reflectance images that had been atmospherically corrected using ATREM (Thompson et al., 2015).

We tested FlexBRDF and refined our code using data acquired from several different sensors over different land cover types (Table 1). The testing was designed to assess the generality of the approach, using sites with significant heterogeneity (Southern California, Yosemite, Fairbanks), moderate variation (Mudumalai) and comparatively homogeneous land cover (Wisconsin). Application of an automated approach to correcting NEON data in particular is necessary, as NEON flies dozens of sites annually using multiple imaging spectrometer payloads, generating over 1000 flightlines per year. Likewise, data from California, India and Alaska were all collected by NASA in support of large airborne campaigns for which single-line corrections are both impractical and likely to generate highly variable results. For all analyses, we used atmospherically corrected reflectance imagery as provided by the data distributor.

Flight box	Date of acquisition	Sensor	Spatial res (m)	Spectral res (nm)	# Bands	Land cover
Southern California 2013	5/22/2013	AVIRIS -C	14.4 - 15.8	10	224	urban, chaparral, oak woodland, conifer forest
Southern California 2016	6/16/2016	AVIRIS -C	14.4 - 15.6	10	224	urban, chaparral, oak woodland, conifer forest
Yosemite, CA	6/7/2017	AVIRIS -C	13.7 - 14.9	10	224	conifer forest, woodland, snow
Fairbanks, AK	7/23/2018	AVIRIS -NG	5.2	5	425	boreal forest
Mudumalai, India	1/5/2016	AVIRIS -NG	4	5	425	subtropical and tropical forest
Chequamegon, WI	9/11/2017	NEON	1	5	425	hardwood and conifer forest

Table 1. Sensor and environmental properties of all test sites. See Table S1 for list of specific flightlines used.

3 Methods

3.1 Topographic Correction

In areas with complex terrain, a topographic correction should be implemented prior to or in conjunction with the BRDF correction (Jia et al., 2020; Schläpfer et al., 2015; Weyermann et al., 2015), since terrain orientation in relation to sun and sensor angles affects image reflectance values (Justice et al., 1981). We corrected for topography on a flightline-by-flightline basis,

following the sun-canopy-sensor with C-correction (SCS+C) described by Soenen et al. (2005). The SCS+C correction combines the C-correction, which assumes consistent geometry of terrain and trees, with normalized SCS geometry. Each pixel is corrected according to its slope, incidence angle, and solar zenith angle:

$$R_t = R\frac{\cos\alpha\cos\theta_s + C}{\cos i + C} \qquad (1)$$

where R_t is topographically-corrected reflectance, R is uncorrected reflectance, α is the terrain slope, θ_s is the solar zenith angle, and i is the solar incidence angle. C is a function of the parameters of the linear relationship observed between R and $\cos i$, shown in Equation 2.

$$R = a + b\cos i \quad \text{and} \quad C = \frac{a}{b} \qquad (2)$$

3.2 Kernels

FlexBRDF uses the Ross and Li kernels (Wanner et al., 1995), which approximate BRDF shapes at varying solar and sensor view and azimuth angles. The Li geometric kernels describe the arrangement of objects; Li sparse refers to sparse vegetation with characteristically prominent shadowing and Li dense refers to dense vegetation. The Ross volumetric kernels describe the distribution of facets (i.e. leaves); Ross thick assumes LAI ≥ 1, while Ross thin assumes LAI < 1. The kernel-based method is a semi-empirical approach, chosen for its computational feasibility, ability to scale spatially, and because it accounts for subpixel heterogeneity in land cover.

We tested four kernel combinations (sparse-thick, sparse-thin, dense-thick, dense-thin) to identify the set of kernels to apply. Our objective was not to thoroughly test the kernels but rather to identify the kernel combinations that produced consistent corrections across our diverse landscapes, namely reduction of the across-track brightness effect. Illustrated graphically, Li-Dense kernels resulted in overcorrection of pixels in the forward scattering direction in comparison to the sparse kernel (Fig. S1), while the difference between thick and thin was negligible. Subsequent implementation exclusively used the Ross-Thick and Li-Sparse kernels, which are widely used in other relevant studies (Schläpfer et al., 2015; Weyermann et al., 2015), and seem to perform most consistently across a wide range of surface conditions. The open source code for our method allows users to select a range of kernels appropriate to their application. Full mathematical formulation for the derivation of kernels (denoted by K) and the weighting coefficients for the kernel (denoted by f) is provided in Wanner et al. (1995).

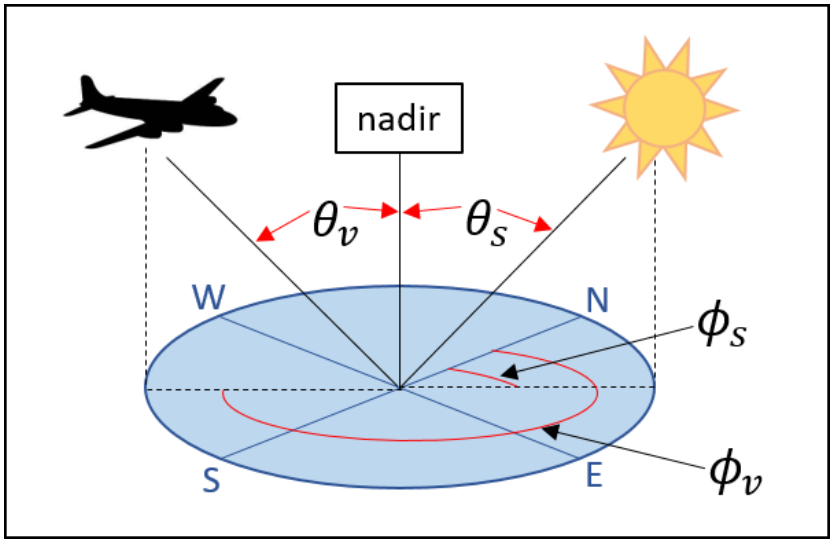

Figure 2. The BRDF is a function of solar view angle (θ_v), solar zenith angle (θ_s), and relative azimuth angle ($\phi = \phi_s - \phi_v$).

3.3 BRDF Correction Model

BRDF is calculated as follows per wavelength and per pixel:

$$\rho(\theta_v,\theta_s,\phi)=f_{iso}+f_{geo}K_{geo}(\theta_v,\theta_s,\phi)+f_{vol}K_{vol}(\theta_v,\theta_s,\phi) \quad (3)$$

where θ_v is the view zenith angle, θ_s is the solar zenith angle, and ϕ is the relative azimuth angle (Fig. 2). The K parameters are the kernel values, which are fixed values derived for each wavelength and are a function of each pixel's combination of view and solar angles. The f values are the least squares regression coefficients (referred to here as BRDF coefficients) that account for varying vegetation structure in the sampled pixels. The set of geometric, volumetric, and isotropic weighting coefficients - f_{iso}, f_{geo}, f_{vol} - describe a characteristic land cover type. For this reason, BRDF corrections generally use a pre-classification scheme or alternatively an index (e.g. Schläpfer et al., 2015) or, in our case, NDVI binning.

The BRDF correction approximates nadir ($\theta_v=0$) reflectance for each pixel based on the calculated kernel values and derived BRDF coefficients. When $\theta_v=0$, $\phi_v$becomes arbitrary. As such, we use a relative azimuth angle that is normalized to an arbitrary number (ϕ_n). Equation 4 describes the application of the correction factors, which compare the observed reflectance of a pixel (or, in this case, the topographically-corrected reflectance R_t) to the modeled reflectance at nadir. These factors are calculated and applied on a per-wavelength and per-pixel basis, outputting topographic- and BRDF-corrected reflectance R_{tb}.

$$R_{tb}=R_t(0,\theta_s,\phi_n)=R_t(\theta_v,\theta_s,\phi)\frac{\rho(0,\theta_s,\phi_n)}{\rho(\theta_v,\theta_s,\phi)} \quad (4)$$

3.4 NDVI Stratification

Pre-correction stratification of imagery is often used in BRDF correction to ensure that correction coefficients capture differences in vegetation canopy characteristics (e.g., structure, leaf shape, leaf area, etc.) (Colgan et al., 2012; Jensen et al., 2018; Jia et al., 2020; Schläpfer et al., 2015; Weyermann et al., 2015). Rather than a discrete classification scheme, we use a vegetation index, which can facilitate a continuous stratification of vegetation. Reflectance image pixels were binned based on NDVI calculated as $(R_{850}\text{-}R_{665})/(R_{850}+R_{665})$. To assess the effect of NDVI bin size on the corrected results, we ran BRDF corrections with 3, 8, and 18 bins for values of NDVI > 0.05 (Table 2). Once binned, BRDF coefficients were calculated using Equation 4 for each NDVI bin separately.

Initial tests used static predefined bins (Table 2) in which we masked out pixels with very low NDVI values (< 0.05) to account for water, non-vegetation and anomalous values. For output maps, original reflectance values were retained in the BRDF-corrected product in masked areas. After testing, we also implemented a dynamic binning approach that utilized 18 bins with divisions of equal sample size within the range of 0.05 < NDVI < 0.9. This approach aimed to accommodate images in which NDVI variability was within a narrow range, such as in the NEON Wisconsin box used in our study (Fig. S2).

Like a cover type classification, there is the risk of abrupt boundaries in BRDF-corrected reflectance at transitions between NDVI bins. To prevent edge effects between NDVI classes in the corrected imagery, we tested smoothing techniques between bins for the weighting factors using the most numerous bin approach (18-bin). We tested: unweighted linear regression (where coefficients are modeled as a function of NDVI), weighted linear regression (based on the size of the bin), and linear interpolation using the Python SciPy library (Virtanen et al., 2020). To avoid overcorrection in very low (0.05-0.25) and very high (0.85-1) NDVI, smoothing methods were applied only on bins between 0.25 and 0.85.

# bins	Bin boundaries
3	0.3, 0.7
8	0.2, 0.3, 0.4, 0.5, 0.6, 0.7, 0.8
18	0.1, 0.15, 0.2, 0.25, 0.3, 0.35, 0.4, 0.45, 0.5, 0.55, 0.6, 0.65, 0.7, 0.75, 0.8, 0.85, 0.9

Table 2. NDVI value divisions for the static NDVI bin approach

Although we only compared corrections using NDVI bins, our open-source code can accommodate a user-supplied classification or use an alternate vegetation index to NDVI.

3.5 Reference Solar Zenith Angle

In general, correcting BRDF for a single flightline models nadir-viewing reflectance ($\theta_v=0$) for each pixel based on the solar zenith angle (θ_s) at the time of flight. For flight boxes in which lines are acquired over multiple hours within a day, this correction approach introduces systematic line-to-line brightness differences. FlexBRDF thus corrects all lines within a flight box to a reference solar zenith angle (θ_{sr}) (Chen et al., 1999; Colgan et al., 2012; Weyermann et

al., 2015). As such, θ_s can be substituted for θ_{sr} in Equation 4 to output topographic- and BRDF-corrected reflectance with solar zenith reference R_{tbz} (Equation 5).

$$R_{tbz} = R_t(0, \theta_{sr}, \phi_n) = R_t(\theta_v, \theta_s, \phi) \frac{\rho(0, \theta_{sr}, \phi_n)}{\rho(\theta_v, \theta_s, \phi)} \quad (5)$$

The selection of θ_{sr} for a flight box is not straightforward, especially if analyses of images from one date are to be integrated with data from images collected on another date. To assess the ramifications, we compared four values of θ_{sr} (Table 3) in our implementation of FlexBRDF for the initial 22 May 2013 Southern California flight box using the 18-bin group with linear interpolation. For all tests, we used the latitude (33.7°) averaged from the center points of all images to determine θ_{sr}. Approach θ_{s1} uses the solar zenith angle at solar noon on the date of acquisition, which could reasonably be considered a default approach for some applications. θ_{s2} uses the average of all solar zenith angles at solar noon across the date range encompassing the growing season, which can be seen as a generalized value suitable for integrating data from multiple dates but risks overcorrecting images with solar view angles that differ substantially from the seasonal average (Zhang et al., 2016). θ_{s3} uses the average observed θ_s from the flight box, which could be considered a relatively cautious default, but could have implications for integrating images across dates. θ_{s4} uses the solar zenith angle at solar noon on the summer solstice, which might also be considered a reasonable baseline for integrating data from across the growing season, but will also always be a value that is at the extreme of observed values for any given flight box. Of note, any approach that uses θ_{sr} tied to solar noon can be problematic if all flightlines are collected before or after noon.

Name	Calculation	Solar zenith angle
θ_{s1}	Solar noon on day of acquisition	13.78
θ_{s2}	Solar noon averaged for growing season	22.22 (April-October) 14.59 (June-August)
θ_{s3}	Observed average θ_s for all lines in flight box	23.87
θ_{s4}	Solar noon on summer solstice	10.37

Table 3. Solar zenith angles in degrees from nadir tested for BRDF correction. Values are provided for the 22 May 2013 image used for initial development of the method. Two periods were tested for θ_{s2}: a broad estimate for growing season (April-October) and a more restricted period (June-August). The April-October period was closer to the flightbox average, and is shown in subsequent results.

3.6 Assessment

First, we qualitatively evaluated spectral continuity across flightlines by inspecting for clear boundaries between images within a flight box or between NDVI stratification classes within an image, both of which would indicate a poor correction. We further assessed spectral consistency and continuity across the flight box through visual inspection of transects. Four transects were drawn across the flight box, oriented perpendicular to the rotation angle of the images (-67° for the California test images). Points were distributed every 500m across each transect. For each point, we calculated the mean reflectance value from a 5 pixel by 5 pixel window to account for possible errors in image registration. We plotted transects for eight bands covering the portion of the VSWIR range that most prominently exhibits BRDF effects (480, 560, 660, 850, 975, 1050, 1150, and 1240 nm). Discontinuities in reflectance values at image boundaries across the transect indicate the presence of residual BRDF effects.

Quantitatively, we performed a direct comparison of pixel values between overlapping areas of adjacent flightlines. Accounting for imperfect spatial registration between overlapping images, we used a moving window to perform spectral matching on adjacent subsets of the image pixels. For the May 2013 Southern California box, we extracted the overlapping pixels for each wavelength of the entire image spectrum, ran a simple linear regression, and calculated the root mean square error (RMSE) and mean absolute deviation (MAD) following Jensen et al. (2018) and Collings et al. (2010). Lower RMSE and MAD indicate a closer match between overlapping areas, and are thus interpreted as a better correction. These metrics were averaged across all overlap areas in a flight box by wavelength. We repeated the method for subsequent test flight boxes using a 10-band spectral subset (480, 560, 660, 850, 975, 1050, 1150, 1240, 1650, and 2215 nm) instead of the full spectrum.

4 Results

4.1 Southern California 2013

Compared to single line processing, grouping of images improved consistency of the shape and pattern of BRDF coefficients by NDVI bin and across wavelengths (Fig. S3). The isotropic coefficient in particular is a good indicator of BRDF model performance because it represents the bidirectional reflectance at $\theta_v=0$ and $\theta_v=0$ for a given pixel (Roujean et al., 1992). For high NDVI pixels, the reflectance should resemble a vegetation spectrum while for low NDVI pixels, it should appear like a soil spectrum. The group method is able to produce physically sound isotropic coefficients while the single line method yields inconsistent, and in some cases, unreasonable results.

All group processing iterations yielded lower RMSE (up to 2.7% less, varying by wavelength) and MAD (up to 2.4% less) in overlap areas than single line processing and uncorrected reflectance (Fig. 4, 5; Table S2). In contrast, all three single processing iterations (3-bin, 8-bin, and 18-bin) yielded higher RMSE (up to 1.1% higher) and MAD (up to 0.7% higher)

than the original reflectance in the red edge/NIR range. The various grouping methods performed similarly across most of the spectrum, but the 3-bin approach yielded the lowest values for RMSE and MAD in the 700 - 1400 nm range. Of the different smoothing methods (Fig. S4), which were only tested on the 18-bin group iteration, the weighted linear regression is the only method that performed noticeably worse across the entire spectrum, especially in the 2000 - 2500 nm range (Fig. S5).

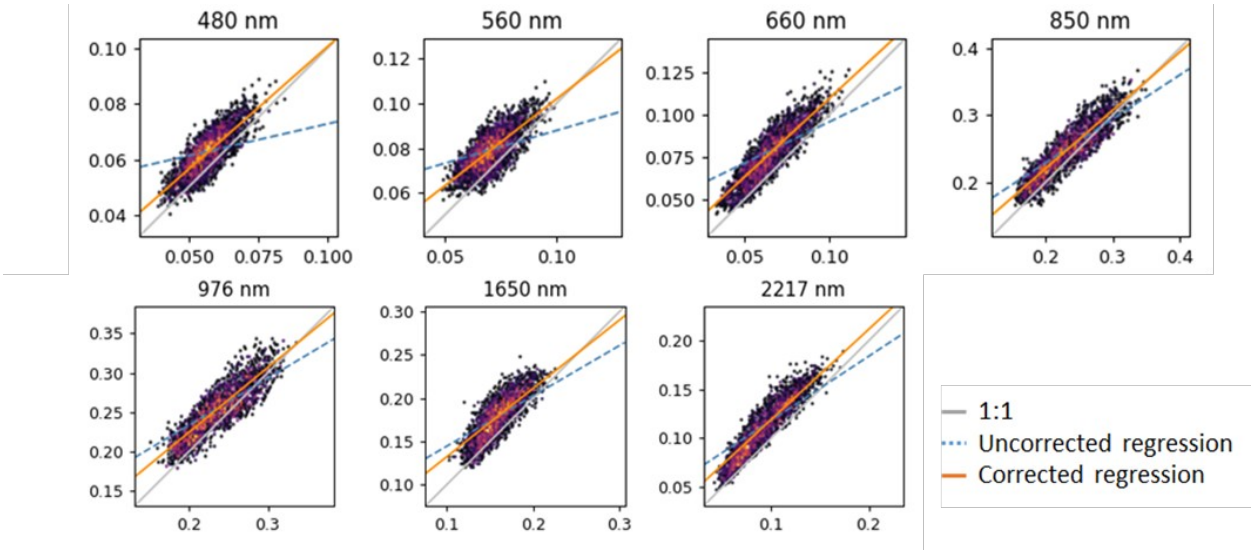

Figure 4. Scatterplots show overlapping reflectance for two lines from the 2013 Southern California flight box. Points are from the corrected images. Perfect spectral consistency would show points falling along the 1:1 line (grey).

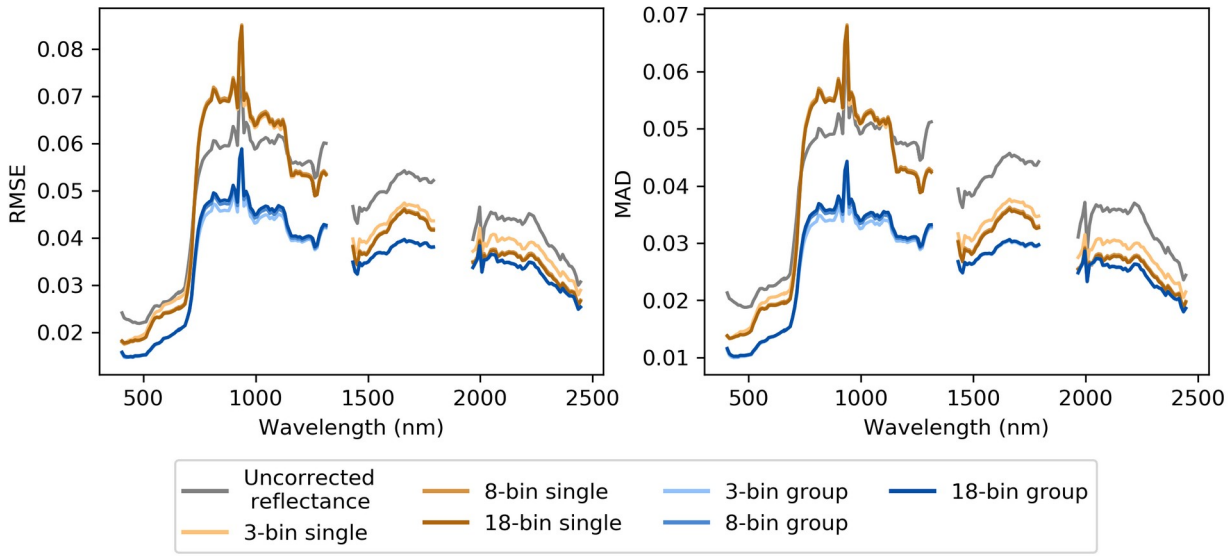

Figure 5. RMSE and MAD from the simple linear regression fit are averaged for all overlapping areas in the flight box and shown for the entire spectrum.

Upon visual inspection, group processing yielded a mosaic with minimized seamlines between adjacent flightlines (Fig. 6). While the number of NDVI bins did not affect the overall appearance of boundaries between flightlines, use of fewer bins resulted in more prominent edges between NDVI classes in the corrected image (Fig. S6). In the use of static bins, we found that smaller and more numerous NDVI bins produced corrections with less evidence of edges among classes or between flightlines. The inclusion of a smoothing method for BRDF coefficients between bins resulted in comparable RMSE and MAD values to unsmoothed coefficients, but also reduced discontinuities across NDVI class boundaries. Spectral data extracted from transects across the flightlines generally exhibited more continuous reflectance values in overlap areas within the corrected images, or, at worse minimal difference from uncorrected data (Fig. 7).

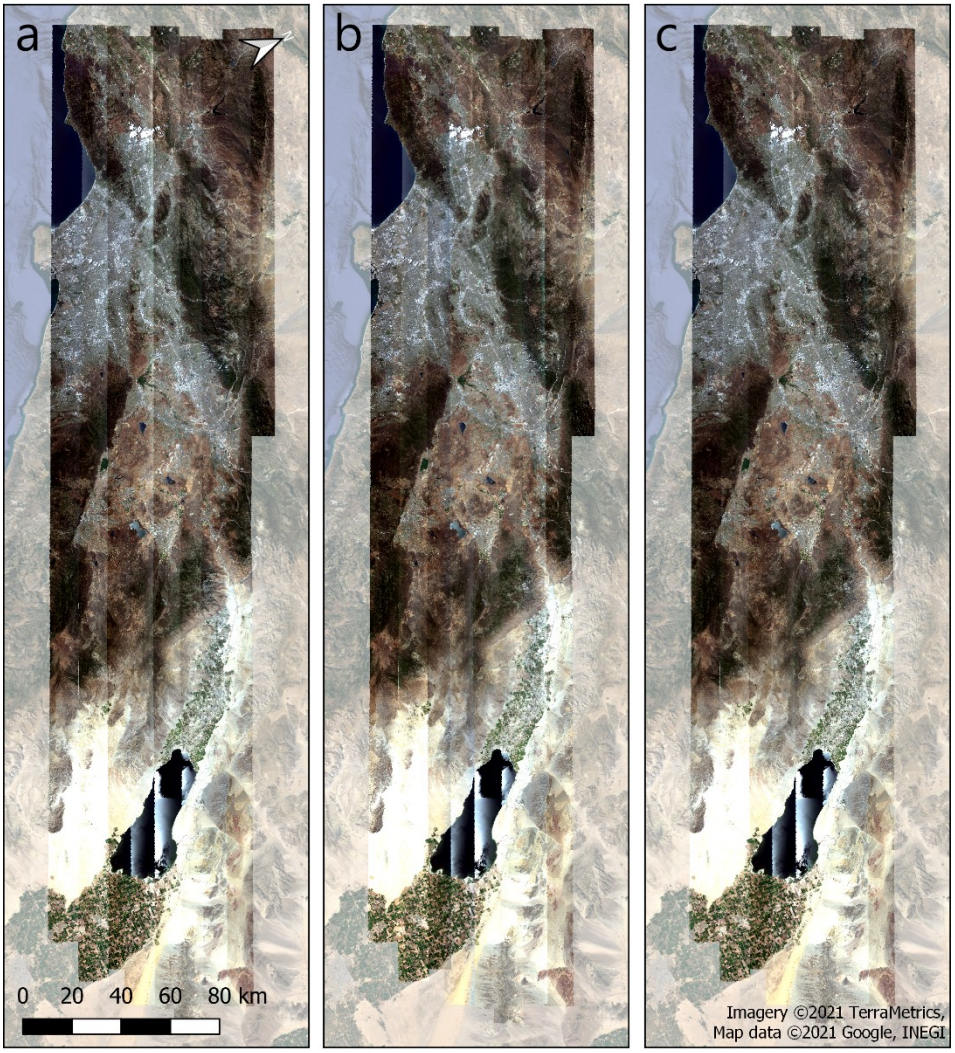

Figure 6. Mosaicked true color reflectance images over Southern California, showing (a) no BRDF correction, (b) 18-bin single correction, and (c) 18-bin group correction.

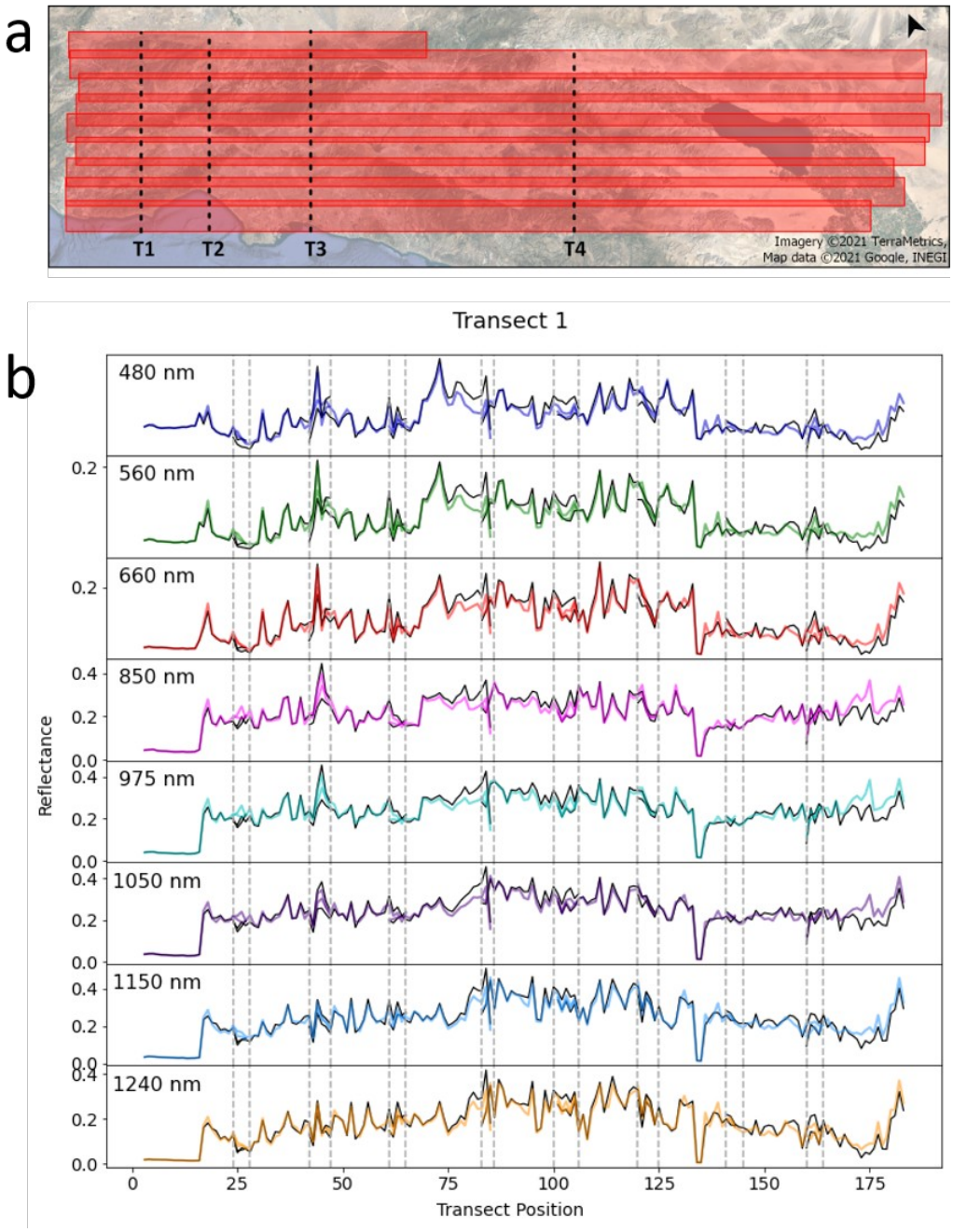

Figure 7. (a) A successfully corrected image should show a continuous transect line. Transects are shown for the Southern California 2013 box. (b) Average reflectance before (black) and after correction (color) is shown along Transect 1, where dotted lines denote overlap regions. Additional transect plots are shown in Fig. S7.

Finally, the inclusion of θ_{sr} improved consistency across the flight box, both visually and in the quantitative assessment. While all four test angles yielded visually smooth mosaics, θ_{s2}

and θ_{s3} resulted in comparably low RMSE and MAD values (up to 0.7% lower than correction with no θ_{sr}) (Fig. 8).

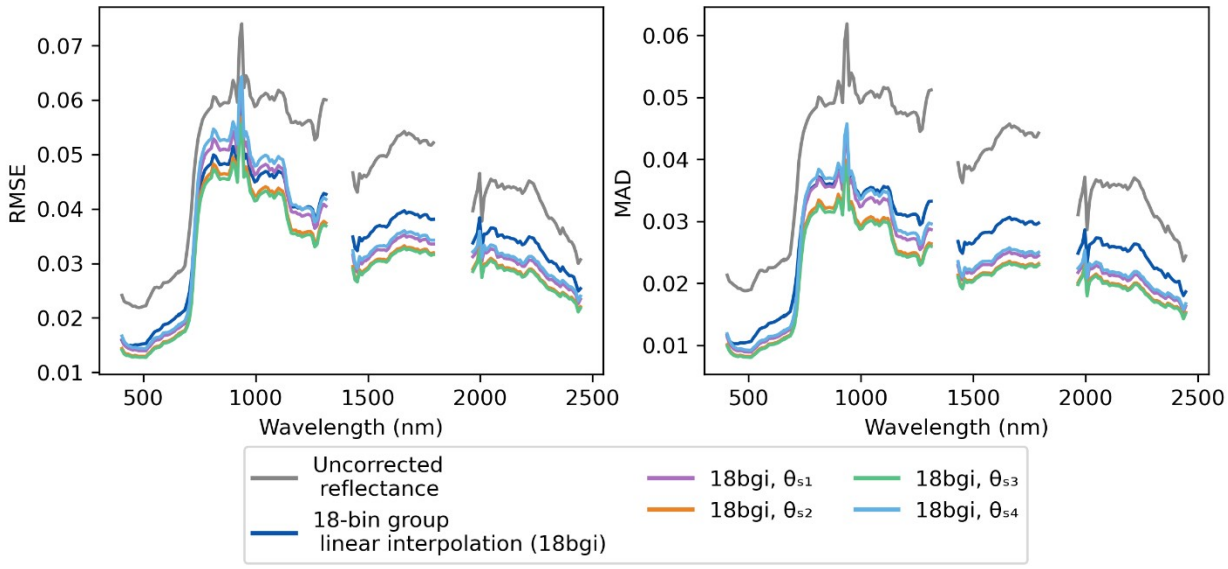

Figure 8. Reference solar zenith angle tests compared to uncorrected reflectance and corrected reflectance with no reference.

4.2 Other Sites

For secondary test sites, we compared 3-bin group, 18-bin group with interpolation (no θ_{sr}), and 18-bin group with interpolation (with θ_{s3}) based on results from 22 May 2013 Southern California imagery. In all sites, all three BRDF correction methods yielded lower RMSE and MAD than uncorrected reflectance (Fig. S8), as well as a visually more continuous mosaic (Fig. 9, S9). The inclusion of θ_{s3} had the largest effect on California boxes, lowering RMSE and MAD for the two Southern California boxes. For the Yosemite box, the inclusion of θ_{s3} performed worse than the 3-bin or 18-bin without θ_{sr}, though it still yielded lower RMSE and MAD than the uncorrected data. The 3-bin and 18-bin group processing yielded similar results for the remaining flightlines regardless of solar zenith reference (Fig. S8). The dynamic binning approach, which aimed to address the small range of NDVI values observed in the NEON Wisconsin box, had virtually no effect on RMSE and MAD (Fig. S10), but is recommended for most applications because it lessens the chance for anomalous results if a fixed bin has a small sample size for computing BRDF coefficients.

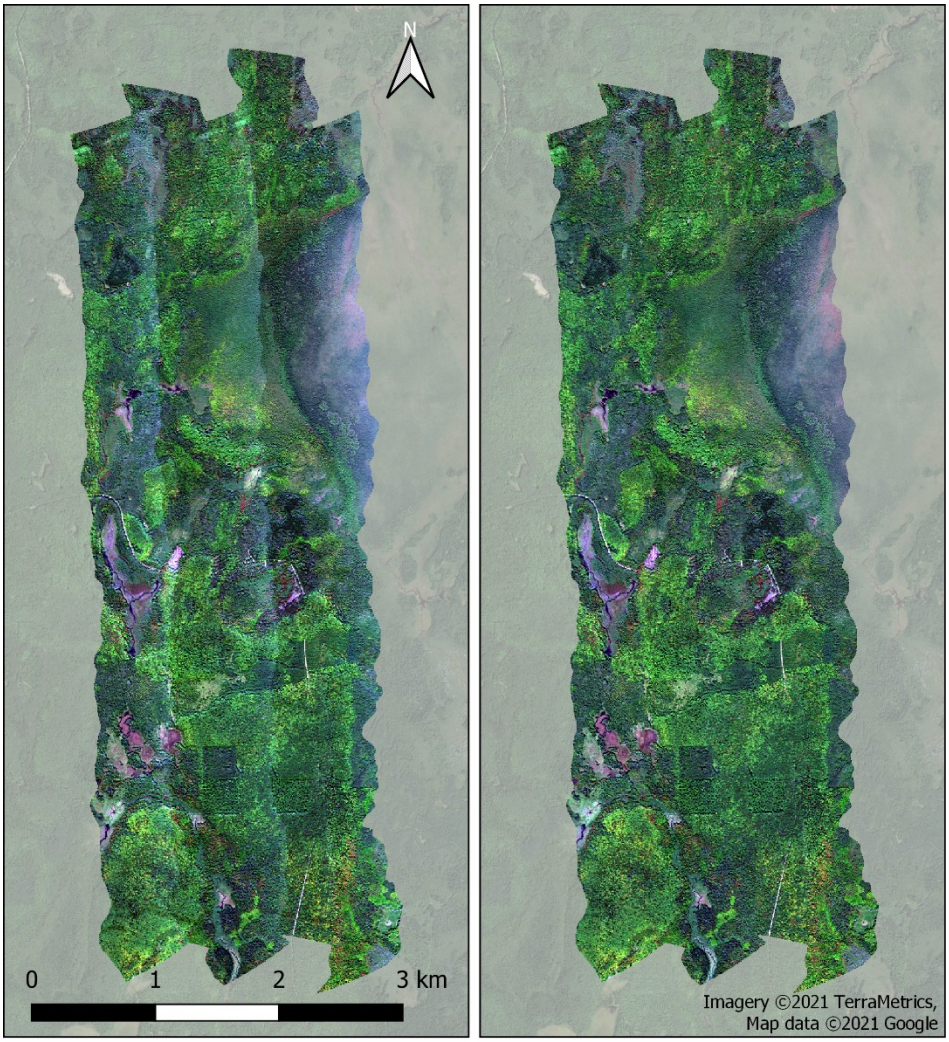

Figure 9. Before (left) and after (right) BRDF correction for the NEON-Wisconsin site. Other sites are shown in Fig. S9.

5 Discussion

Grouping images for BRDF correction ensures a consistent correction across the flight box regardless of variation in land cover within and between flightlines. Due to the flightline size and land cover complexity, we suspect that some single image corrections are too heavily influenced by the proportion and geographic location within a flightline of certain land cover types, such as agriculture. Figure S3 shows evidence of grouped correction producing a more consistent and stable correction than single flightline corrections, while Figure 5 provides quantitative evidence of improved correspondence of image spectra in overlap areas and Figure 6 demonstrates the impacts on mosaic appearance.

Of the correction models we tested on the 22 May 2013 Southern California box, all grouping methods outperformed the single line methods. While the different grouping methods all yielded similar results, the 3-bin and 18-bin grouping methods represented a trade-off: by a small amount, the 3-bin grouping exhibited the lowest RMSE and MAD values in overlap areas,

while the 18-bin grouping produced the most continuous output image, with less evidence of borders and only slightly higher MAD and RMSE. These two grouping methods were comparable for all subsequent test sites. Of the smoothing methods we tested for BRDF coefficients between NDVI bins, linear interpolation resulted in images with minimal seamlines between adjacent flightlines compared to regression approaches and an absence of boundaries between NDVI bins.

We expected that the NEON box would be a unique case because of its constricted range of NDVI values, in which 90% of the NDVI values range between 0.7 and 0.9 (Fig. S2). To avoid numerous NDVI bins with minimal samples for computing BRDF coefficients, we revised our static bin approach to create a dynamic binning approach, where the bins are defined by equal area of an NDVI bin rather than a fixed NDVI bin breadth. However, the test of an 18-bin dynamic group correction yielded RMSE and MAD values that were virtually identical to the static binning (Fig. S10). This suggests that either the static binning or dynamic binning work well in homogeneous landscapes, but we expect that dynamic binning may have advantages in homogeneous landscapes. This could be the basis for further testing; further development could test optimization approaches to dynamically vary the range of factors used in BRDF correction (e.g., including kernel selection).

Establishing a reference solar zenith angle is critical for highly diverse scenes and/or very long flightlines. Of the four angles we tested for the 22 May 2013 Southern California box, we achieved the best results for θ_{s2} and θ_{s3}. The default selection we recommend is θ_{s3}, since this is the most accurate representation of the average solar zenith angle observed on the day of data collection. However, if the user aims to compare flight boxes from the same location acquired on different dates, it may be useful to standardize these boxes to the same angle. In that case, we recommend θ_{s2}. The inclusion of a solar reference angle was beneficial in the second Southern California flight box, but appeared detrimental for the Yosemite box and had negligible impact on the remaining sites (Fig. S8). It is likely that Southern California saw the biggest improvement from the inclusion of a reference solar zenith angle because these lines are exceptionally long, and acquired over a span of many hours (and thus across a large range of solar zenith angles) in one day.

All of our examples used images that overlapped and were acquired on the same day. Future work should test the extent to which these criteria can be extended or should be restricted. First, although it is reasonable to expect that this method would work on flightlines that are in close proximity but not overlapping, it would be difficult to assess model performance without overlapping areas. As well, it would be hard to specify a cutoff time beyond which images should not be processed together, but a separation of several hours affects reflectance in the image due to change in sun angle and even atmospheric conditions. Using a reference solar zenith angle partially rectifies these considerations.

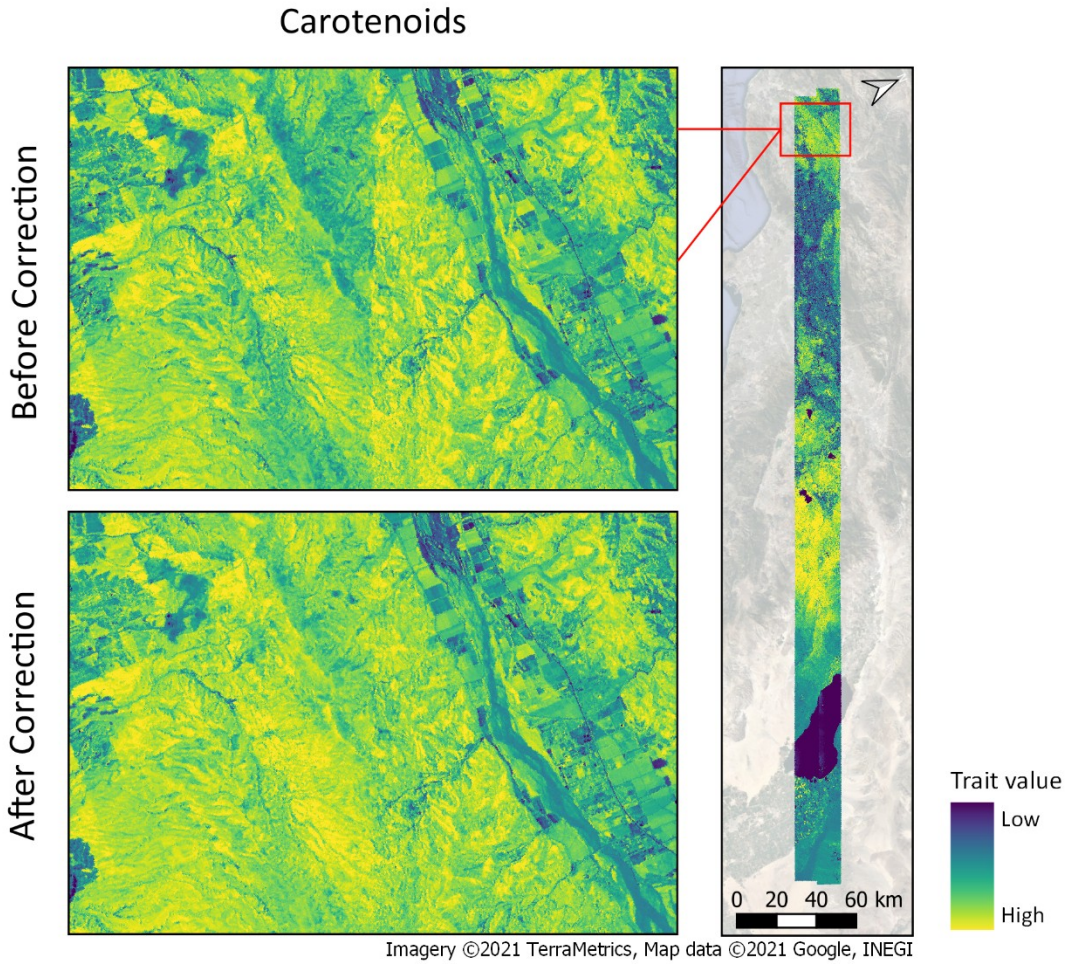

Figure 10. For illustration, a trait map of carotenoids is shown for uncorrected and BRDF-corrected data from two overlapping Southern California flightlines. A clear boundary line runs through the center of the map derived from uncorrected imagery.

Our overall objective for BRDF corrections is to reduce the influence of BRDF on derived maps, such as vegetation composition, fractional cover, disturbance, stress and functional traits. After an appropriate BRDF correction, algorithms that address ecological questions can be applied to generate maps that can be mosaicked with minimal seams. Such applications depend on consistent spectral reflectance across flightlines, and a method such as FlexBRDF can greatly reduce discontinuities between flightlines, as illustrated with a vegetation trait map derived for carotenoids following Singh et al. (2015) (Fig. 10). Some methods are more sensitive to BRDF than others, e.g. trait mapping (Singh et al., 2015) and quantification of biodiversity metrics (Féret & Asner, 2014), while methods that leverage unmixing or spectral angles are less sensitive to per pixel brightness effects. Our code for FlexBRDF has been designed to be adaptable to a range of environments. Although we demonstrate FlexBRDF using a parameterization that we found worked well across many environments, users of FlexBRDF can tune the approach to different kernel combinations, vegetation index, binning approach (the code also enables using a classification layer rather than NDVI bins), and reference solar zenith

angle. It is part of a larger suite of open-source Python tools for processing hyperspectral imagery available at https://github.com/EnSpec/hytools.

6 Conclusion

Current and forthcoming spaceborne imaging spectroscopy missions such as SBG will require extensive airborne data sets for calibration and validation. Data sets of derived products that exhibit artifacts of BRDF and other effects (e.g., Fig. 10) may be problematic for integration with these new spaceborne data. FlexBRDF will allow users to mosaic maps of vegetation properties derived from imaging spectroscopy on groups of adjacent airborne flightlines without stark image boundaries created by BRDF effects. We demonstrate that FlexBRDF is highly applicable for airborne hyperspectral imagery covering diverse environments. However, our open source code is written such that users can implement and test a wide range of BRDF approaches. Our final recommendation is to group the images, stratify the data with 18 NDVI bins, use the solar zenith angle from the flight box center point as a reference, and smooth the coefficients with linear interpolation. While these parameters worked well on most sites (although Yosemite may benefit from a different solar zenith reference), the method is flexible and the user may adjust the parameters to fit their needs.

Acknowledgments

The research presented here results from testing conducted over multiple years with support from multiple sources. AVIRIS-Classic, AVIRIS-NG, and NEON imagery were accessed from their respective data portals: https://aviris.jpl.nasa.gov/dataportal/, https://avirisng.jpl.nasa.gov/dataportal/, and https://data.neonscience.org/. NQ was primarily supported by the National Science Foundation Graduate Research Fellowship Program under Grant No. DGE-1747503. Any opinions, findings, and conclusions or recommendations expressed in this material are those of the author(s) and do not necessarily reflect the views of the National Science Foundation. Support was also provided by the Graduate School and the Office of the Vice Chancellor for Research and Graduate Education at the University of Wisconsin- Madison with funding from the Wisconsin Alumni Research Foundation. Additional support was provided by NSF Macrosystems Biology Grant 1638720, NASA AIST Grant 80NSSC20K0208, NASA Terrestrial Ecology Grant 80NSSC19M0115, NASA Biodiversity Grant 80NSSC17K0677, and USDA Hatch and McIntire-Stennis Awards WIS01874 and WIS03008. The research carried out at the Jet Propulsion Laboratory, California Institute of Technology, was under a contract with the National Aeronautics and Space Administration (80NM0018D0004). Government sponsorship is acknowledged.

References

Asner, G. P., Brodrick, P. G., Anderson, C. B., Vaughn, N., Knapp, D. E., & Martin, R. E. (2016). Progressive forest canopy water loss during the 2012–2015 California drought. *Proceedings of the National Academy of Sciences*, *113*(2), E249-E255.

Asner, G. P., Martin, R. E., Anderson, C. B., & Knapp, D. E. (2015). Quantifying forest canopy traits: Imaging spectroscopy versus field survey. *Remote Sensing of Environment*, *158*, 15–27. https://doi.org/10.1016/j.rse.2014.11.011

Bhattacharya, B. K., Green, R. O., Rao, S., Saxena, M., Sharma, S., Ajay Kumar, K., Srinivasulu, P., Sharma, S., Dhar, D., Bandyopadhyay, S., Bhatwadekar, S., & Kumar, R. (2019). An overview of AVIRIS-NG airborne hyperspectral science campaign over India. *Current Science*, *116*(7), 1082. https://doi.org/10.18520/cs/v116/i7/1082-1088

Buchhorn, M., Raynolds, M. K., & Walker, D. A. (2016). Influence of BRDF on NDVI and biomass estimations of Alaska Arctic tundra. *Environmental Research Letters*, *11*(12), 125002. https://doi.org/10.1088/1748-9326/11/12/125002

Chen, J. M., Leblanc, S. G., Miller, J. R., Freemantle, J., Loechel, S. E., Walthall, C. L., Innanen, K. A., & White, H. P. (1999). Compact Airborne Spectrographic Imager (CASI) used for mapping biophysical parameters of boreal forests. *Journal of Geophysical Research: Atmospheres*, *104*(D22), 27945–27958. https://doi.org/10.1029/1999JD900098

Colgan, M., Baldeck, C., Féret, J.-B., & Asner, G. (2012). Mapping savanna tree species at ecosystem scales using support vector machine classification and BRDF correction on airborne hyperspectral and LiDAR data. *Remote Sensing*, *4*(11), 3462–3480. https://doi.org/10.3390/rs4113462

Collings, S., Caccetta, P., Campbell, N., & Wu, X. (2010). Techniques for BRDF correction of hyperspectral mosaics. *IEEE Transactions on Geoscience and Remote Sensing*, *48*(10), 3733–3746. https://doi.org/10.1109/TGRS.2010.2048574

Dennison, P. E., Qi, Y., Meerdink, S. K., Kokaly, R. F., Thompson, D. R., Daughtry, C. S. T., Quemada, M., Roberts, D. A., Gader, P. D., Wetherley, E. B., Numata, I., & Roth, K. L. (2019). Comparison of methods for modeling fractional cover using simulated satellite hyperspectral imager spectra. *Remote Sensing*, *11*(18), 2072. https://doi.org/10.3390/rs11182072

Féret, J.-B., & Asner, G. P. (2014). Mapping tropical forest canopy diversity using high-fidelity imaging spectroscopy. *Ecological Applications*, *24*(6), 1289–1296. https://doi.org/10.1890/13-1824.1

Green, R. O., Eastwood, M. L., Sarture, C. M., Chrien, T. G., Aronsson, M., Chippendale, B. J., Faust, J. A., Pavri, B. E., Chovit, C. J., Solis, M., Olah, M. R., & Williams, O. (1998). Imaging spectroscopy and the Airborne Visible/Infrared Imaging Spectrometer (AVIRIS). *Remote Sensing of Environment*, *65*(3), 227–248. https://doi.org/10.1016/S0034-4257(98)00064-9

Guerschman, J. P., Hill, M. J., Renzullo, L. J., Barrett, D. J., Marks, A. S., & Botha, E. J. (2009). Estimating fractional cover of photosynthetic vegetation, non-photosynthetic vegetation and bare soil in the Australian tropical savanna region upscaling the EO-1 Hyperion and MODIS sensors. *Remote Sensing of Environment*, *113*(5), 928–945. https://doi.org/10.1016/j.rse.2009.01.006

Hamlin, L., Green, R. O., Mouroulis, P., Eastwood, M., Wilson, D., Dudik, M., & Paine, C. (2011). Imaging spectrometer science measurements for terrestrial ecology: AVIRIS and

new developments. *2011 Aerospace Conference*, 1–7. https://doi.org/10.1109/AERO.2011.5747395

Hueni, A., McCubbin, I., Schuettemeyer, D., Green, R. O., Hook, S. J., Schaepman, M. E., & Margolis, H. A. (2018). AVIRIS-NG and APEX airborne imaging spectrometer campaigns in support of ESA satellite CAL/VAL and simulation. *American Geophysical Union, Fall Meeting 2018*.

Iwasaki, A., Ohgi, N., Tanii, J., Kawashima, T., & Inada, H. (2011). Hyperspectral Imager Suite (HISUI) -Japanese hyper-multi spectral radiometer. *2011 IEEE International Geoscience and Remote Sensing Symposium*, 1025–1028. https://doi.org/10.1109/IGARSS.2011.6049308

Jensen, D. J., Simard, M., Cavanaugh, K. C., & Thompson, D. R. (2018). Imaging spectroscopy BRDF Correction for mapping Louisiana's coastal ecosystems. *IEEE Transactions on Geoscience and Remote Sensing*, *56*(3), 1739–1748. https://doi.org/10.1109/TGRS.2017.2767607

Jetz, W., Cavender-Bares, J., Pavlick, R., Schimel, D., Davis, F. W., Asner, G. P., Guralnick, R., Kattge, J., Latimer, A. M., Moorcroft, P., Schaepman, M. E., Schildhauer, M. P., Schneider, F. D., Schrodt, F., Stahl, U., & Ustin, S. L. (2016). Monitoring plant functional diversity from space. *Nature Plants*, *2*(3), 16024. https://doi.org/10.1038/nplants.2016.24

Jia, W., Pang, Y., Tortini, R., Schläpfer, D., Li, Z., & Roujean, J.-L. (2020). A Kernel-Driven BRDF approach to correct airborne hyperspectral imagery over forested areas with rugged topography. *Remote Sensing*, *12*(3), 432. https://doi.org/10.3390/rs12030432

Justice, C. O., Wharton, S. W., & Holben, B. N. (1981). Application of digital terrain data to quantify and reduce the topographic effect on Landsat data. *International Journal of Remote Sensing*, *2*(3), 213–230. https://doi.org/10.1080/01431168108948358

Kampe, T. U. (2010). NEON: The first continental-scale ecological observatory with airborne remote sensing of vegetation canopy biochemistry and structure. *Journal of Applied Remote Sensing*, *4*(1), 043510. https://doi.org/10.1117/1.3361375

Kasischke, E. S., Goetz, S. J., Kimball, J. S., & Mack, M. M. (2010). *The Arctic-Boreal Vulnerability Experiment (ABoVE): A Concise Plan for a NASA-Sponsored Field Campaign* (Final Report on the VuRSAL/ABoVE Scoping Study).

Lee, C. M., Cable, M. L., Hook, S. J., Green, R. O., Ustin, S. L., Mandl, D. J., & Middleton, E. M. (2015). An introduction to the NASA Hyperspectral InfraRed Imager (HyspIRI) mission and preparatory activities. *Remote Sensing of Environment*, *167*, 6–19. https://doi.org/10.1016/j.rse.2015.06.012

Li, L., Ustin, S. L., & Lay, M. (2005). Application of multiple endmember spectral mixture analysis (MESMA) to AVIRIS imagery for coastal salt marsh mapping: A case study in China Camp, CA, USA. *International Journal of Remote Sensing*, *26*(23), 5193–5207. https://doi.org/10.1080/01431160500218911

Loizzo, R., Guarini, R., Longo, F., Scopa, T., Formaro, R., Facchinetti, C., & Varacalli, G. (2018). Prisma: The Italian Hyperspectral Mission. *IGARSS 2018 - 2018 IEEE International Geoscience and Remote Sensing Symposium*, 175–178. https://doi.org/10.1109/IGARSS.2018.8518512

National Academies of Sciences, Engineering, and Medicine (U.S.), (Eds.). (2018). *Thriving on our changing planet: A decadal strategy for Earth observation from space*. The National Academies Press.

Nicodemus, F. E., Richmond, J. C., & Hsia, J. J. (1977). *Geometrical considerations and nomenclature for reflectance*. U.S. Dept. Commerce, Nat. Bureau Standards.

Nieke, J., & Rast, M. (2018). Towards the Copernicus Hyperspectral Imaging Mission for the Environment (CHIME). *IGARSS 2018 - 2018 IEEE International Geoscience and Remote Sensing Symposium*, 157–159. https://doi.org/10.1109/IGARSS.2018.8518384

Roberts, D. A., Gardner, M., Church, R., Ustin, S., Scheer, G., & Green, R. O. (1998). Mapping chaparral in the Santa Monica Mountains using multiple endmember spectral mixture models. *Remote Sensing of Environment*, *65*(3), 267–279. https://doi.org/10.1016/S0034-4257(98)00037-6

Roberts, D. A., Smith, M. O., & Adams, J. B. (1993). Green vegetation, nonphotosynthetic vegetation, and soils in AVIRIS data. *Remote Sensing of Environment*, *44*(2–3), 255–269. https://doi.org/10.1016/0034-4257(93)90020-X

Roujean, J.-L., Leroy, M., & Deschamps, P.-Y. (1992). A bidirectional reflectance model of the Earth's surface for the correction of remote sensing data. *Journal of Geophysical Research*, *97*(D18), 20455. https://doi.org/10.1029/92JD01411

Schaepman-Strub, G., Schaepman, M. E., Painter, T. H., Dangel, S., & Martonchik, J. V. (2006). Reflectance quantities in optical remote sensing—Definitions and case studies. *Remote Sensing of Environment*, *103*(1), 27–42. https://doi.org/10.1016/j.rse.2006.03.002

Schimel, D., Townsend, P. A., & Pavlick, R. (Eds.). (2020). Prospects and pitfalls for spectroscopic remote sensing of biodiversity at the global scale. In *Remote Sensing of*

Plant Biodiversity. Springer International Publishing. https://doi.org/10.1007/978-3-030-33157-3

Schläpfer, D., Richter, R., & Feingersh, T. (2015). Operational BRDF effects correction for wide-field-of-view optical scanners (BREFCOR). *IEEE Transactions on Geoscience and Remote Sensing*, *53*(4), 1855–1864. https://doi.org/10.1109/TGRS.2014.2349946

Schneider, F. D., Morsdorf, F., Schmid, B., Petchey, O. L., Hueni, A., Schimel, D. S., & Schaepman, M. E. (2017). Mapping functional diversity from remotely sensed morphological and physiological forest traits. *Nature Communications*, *8*(1), 1441. https://doi.org/10.1038/s41467-017-01530-3

Serbin, S. P., Singh, A., Desai, A. R., Dubois, S. G., Jablonski, A. D., Kingdon, C. C., Kruger, E. L., & Townsend, P. A. (2015). Remotely estimating photosynthetic capacity, and its response to temperature, in vegetation canopies using imaging spectroscopy. *Remote Sensing of Environment*, *167*, 78–87. https://doi.org/10.1016/j.rse.2015.05.024

Singh, A., Serbin, S. P., McNeil, B. E., Kingdon, C. C., & Townsend, P. A. (2015). Imaging spectroscopy algorithms for mapping canopy foliar chemical and morphological traits and their uncertainties. *Ecological Applications*, *25*(8), 2180–2197. https://doi.org/10.1890/14-2098.1

Soenen, S. A., Peddle, D. R., & Coburn, C. A. (2005). SCS+C: A modified Sun-canopy-sensor topographic correction in forested terrain. *IEEE Transactions on Geoscience and Remote Sensing*, *43*(9), 2148–2159. https://doi.org/10.1109/TGRS.2005.852480

Stuffler, T., Kaufmann, C., Hofer, S., Förster, K. P., Schreier, G., Mueller, A., Eckardt, A., Bach, H., Penné, B., Benz, U., & Haydn, R. (2007). The EnMAP hyperspectral imager—An

advanced optical payload for future applications in Earth observation programmes. *Acta Astronautica*, *61*(1–6), 115–120. https://doi.org/10.1016/j.actaastro.2007.01.033

Thompson, D. R., Gao, B.-C., Green, R. O., Roberts, D. A., Dennison, P. E., & Lundeen, S. R. (2015). Atmospheric correction for global mapping spectroscopy: ATREM advances for the HyspIRI preparatory campaign. *Remote Sensing of Environment*, *167*, 64–77. https://doi.org/10.1016/j.rse.2015.02.010

Veraverbeke, S., Stavros, E. N., & Hook, S. J. (2014). Assessing fire severity using imaging spectroscopy data from the Airborne Visible/Infrared Imaging Spectrometer (AVIRIS) and comparison with multispectral capabilities. *Remote Sensing of Environment*, *154*, 153–163. https://doi.org/10.1016/j.rse.2014.08.019

Virtanen, P., Gommers, R., Oliphant, T. E., Haberland, M., Reddy, T., Cournapeau, D., Burovski, E., Peterson, P., Weckesser, W., Bright, J., van der Walt, S. J., Brett, M., Wilson, J., Millman, K. J., Mayorov, N., Nelson, A. R. J., Jones, E., Kern, R., Larson, E., … van Mulbregt, P. (2020). SciPy 1.0: Fundamental algorithms for scientific computing in Python. *Nature Methods*, *17*(3), 261–272. https://doi.org/10.1038/s41592-019-0686-2

Wang, Z., Chlus, A., Geygan, R., Ye, Z., Zheng, T., Singh, A., Couture, J. J., Cavender‐Bares, J., Kruger, E. L., & Townsend, P. A. (2020). Foliar functional traits from imaging spectroscopy across biomes in eastern North America. *New Phytologist*, *228*(2), 494–511. https://doi.org/10.1111/nph.16711

Wang, Z., Townsend, P. A., Schweiger, A. K., Couture, J. J., Singh, A., Hobbie, S. E., & Cavender-Bares, J. (2019). Mapping foliar functional traits and their uncertainties across three years in a grassland experiment. *Remote Sensing of Environment*, *221*, 405–416. https://doi.org/10.1016/j.rse.2018.11.016

Wanner, W., Li, X., & Strahler, A. H. (1995). On the derivation of kernels for kernel-driven models of bidirectional reflectance. *Journal of Geophysical Research*, *100*(D10), 21077. https://doi.org/10.1029/95JD02371

Weyermann, J., Kneubuhler, M., Schläpfer, D., & Schaepman, M. E. (2015). Minimizing reflectance anisotropy effects in airborne spectroscopy data using Ross–Li model inversion with continuous field land cover stratification. *IEEE Transactions on Geoscience and Remote Sensing*, *53*(11), 5814–5823. https://doi.org/10.1109/TGRS.2015.2415872

Zhang, H. K., Roy, D. P., & Kovalskyy, V. (2016). Optimal solar geometry definition for global long-term landsat time-series bidirectional reflectance normalization. *IEEE Transactions on Geoscience and Remote Sensing*, *54*(3), 1410–1418. https://doi.org/10.1109/TGRS.2015.2480684